# An ultrasensitive photoelectrochemical immunosensor for carcinoembryonic antigen detection based on cobalt borate nanosheet array and $Mn_2O_3$@Au nanocube

Wenbo Lu [a,*,1], Shoufeng Xue [a,1], Xuebo Liu [a], Cancan Bao [a], Huanhuan Shi [b,*]

[a] *Key Laboratory of Magnetic Molecules and Magnetic Information Materials (Ministry of Education), School of Chemistry and Material Science, Shanxi Normal University, Taiyuan 030031, China*

[b] *Institut für Quanten Materialien and Technologien (IQMT), Karlsruher Institut für Technologie (KIT), Hermann-v.-Helmholtz-Platz 1, 76344 Eggenstein-Leopoldshafen, Germany*

ARTICLE INFO

*Keywords:*
Cobalt-borate nanosheet
$Mn_2O_3$@Au nanocube
Arrays
Carcinoembryonic antigen
Photoelectrochemical immunosensor

ABSTRACT

Highly sensitive and selective method of determination for carcinoembryonic antigen (CEA) is of important significance for the effective early diagnosis and treatment of cancer. In this work, we report an ultrasensitive sandwich photoelectrochemical (PEC) immunosensor for CEA detection. To be precise, cobalt-borate nanosheet arrays (Co-Bi NSs) with the larger specific surface area are prepared by electrodeposition and used as the basal material to capture the primary antibody ($Ab_1$) for the first time. And the other photoactive material $Mn_2O_3$@Au nanocube is exploited for labeling the secondary antibody ($Ab_2$). The coulomb force of $Mn_2O_3$@Au nanocube and Co-Bi NSs photoelectrodes as the driving force effectively improves the photoelectric response. Under the light irradiation, charge separation occurs at the same time between AuNPs and $Mn_2O_3$, and the energy levels of $Mn_2O_3$@Au and Co-Bi NSs are effectively matched, achieving the high PEC performance of the biosensor. The synthesized nanomaterials are physically characterized by a series of characterization techniques. Besides, ascorbic acid (AA) is employed as an excellent electron donor, which can inhibit the recombination process of photogenerated electrons and holes, then obtaining enhanced and stable photocurrent signals. Under the optimal experimental conditions, the immunosensor shows a lower detection limit of 5.0 pg $mL^{-1}$ (S/N 3), a wider linear range of 0.1 ng $mL^{-1}$ ~ 1000 ng $mL^{-1}$, as well as excellent specificity, stability and reproducibility. Additionally, as-constructed PEC immunosensor can be applied to detect CEA in human serum, this proposed strategy may afford a promising approach for the biomarker sensing and clinical applications.

## 1. Introduction

Currently, the cancer diseases remain one of the major threat to human health as their effective treatment options remain a huge challenge [1,2]. Thus, the detection for tumor biomarkers, which express the presence or recurrence of cancer, is of important significance for the effective early diagnosis and treatment of cancer [3,4]. Carcinoembryonic antigen (CEA), as the biomarker for many cancers, like colorectal cancer, breast cancer, and ovarian carcinoma, is at the normal level of 3 ~ 5 ng mL $^{1}$ in healthy adults [5–8]. At present, plenty of analytical techniques based on luminescence [9], fluorescence [10], electrochemiluminescence [11], electrochemical [12] and photoelectrochemical (PEC) [13] have been developed to realize the sensitive and efficient recognition of CEA. Among these reported methods, the PEC sensing has been seen as a reliable biological analysis for its desirable advantages and promising potential [14,15].

The PEC bio-analysis uses light for signal generation and electricity for detection signal respectively, and combines the superiorities of optical and electrochemical methods, greatly reducing the cost of instrument [16,17]. In addition, owing to the different energy forms of the input signal source and the output signal, the PEC technique possesses potentially lower background signal and higher sensitivity than the ordinary electrochemical methods [17]. One of the most effective ways to improve the analytical performance of PEC immunosensors is to reduce the background signal while being able to enhance the photocurrent intensity. As an excellent electron donor, ascorbic acid (AA) can inhibit

* Corresponding authors.
*E-mail addresses:* luwb@sxnu.edu.cn (W. Lu), huanhuan.shi@kit.edu (H. Shi).
[1] W. Lu and S. Xue contributed equally to this work.

the recombination process of photogenerated electrons and holes, then obtaining enhanced and stable photocurrent signals [18,19]. In addition, PEC sensor detection instrument is a simple, low cost, rapid and high throughput bioassay [20,21]. Therefore, this technique is promising for analytical applications and has attracted considerable research attention.

Increasing research effort has been focused on the design of the photoactive nanomaterials, since photoactive nanomaterials have unpredictable effect on the photoelectric conversion efficiency and analytical performance of the PEC sensor [22–25]. At present, numerous photosensitive nanomaterials, such as PbS [19], CdSe [26], ZnO [27], CuO [28] and so on have been used to construct PEC immunosensors. However, it is difficult to screen the nanomaterials that can successfully construct energy level matching and have brilliant photoelectric performance. To performance this, recently, transition-metal borates (TMBi) have been widely concerned by researchers, on account of their nontoxic, low cost and abundant reserve on earth [29–33]. For example, Sun et al. synthesized nickel-borate nanoarray supported on carbon cloth (Ni-Bi/CC) as a highly 3D electrode for water oxidation [34]. In 2017, Hyounmyung and his co-workers firstly considered several molybdenum borides as alternative non-noble metal catalysts for the hydrogen evolution reaction (HER) [35]. Luo's group reported an amorphous core–shell like cobalt borate nanosheet-coated cobalt boride hybride (Co-B@Co-Bi), exhibiting remarkable oxygen evolution reaction (OER) [36]. However, there are few works on the application of TMBi in PEC immunosensors. $Mn_2O_3$ nanocubes would be a good candidate for persistent contaminants degradation by photocatalysis [37]. Under visible light irradiation, the electrons (e ) ARE excited from VB of $Mn_2O_3$ and then transferred to the CB, leaving holes (h+) in the VB. Based on the excellent photoelectric performance of $Mn_2O_3$ nanocubes, we have designed and prepared a photoelectrochemical immunosensor.

In this contribution, a novel signal amplification strategy is proposed to construct an ultrasensitive PEC immunosensor, in which cobalt-borate nanosheet arrays (Co-Bi NSs) are worked as the substrate for the first time and carcinoembryonic detection antibody ($Ab_2$)-AuNPs/$Mn_2O_3$ as the label. Specifically, Co-Bi NSs are grown on the Ti mesh (TM) via the electrochemical deposition method. Co-Bi NSs show good photostability, large photoactive area and high loading capacity, can support more photoactive substances, laying a foundation for improving the intensity of photocurrent. Under the light irradiation, charge separation occurs at the same time between AuNPs and $Mn_2O_3$, and the energy levels of $Mn_2O_3$@Au and Co-Bi NSs are effectively matched. Then, electrons are allowed to transfer rapidly from $Mn_2O_3$@Au in the excited state to Co-Bi, and these electrons are collected as the photocurrent eventually, resulting in the amplification of the detected photocurrent signal. When $Mn_2O_3$@Au composition is served as an immune probe to label $Ab_2$, AuNPs bind the labeled antibody $Ab_2$ through Au-N bond. Based on the sandwich PEC immunosensor, fabricated by the specific combination of antigen–antibody immune reaction, the reliable recognition and efficient signal amplification of CEA can be realized.

## 2. Experimental section

### 2.1. Synthesis of Co-Bi nanosheet arrays

Co-Bi nanosheet arrays (NSs) are formed by electrodeposition on a Ti mesh (TM). Before the experiment, the TM (1 cm × 4 cm) is ultrasonically washed with 3 M of HCl, acetone, and water for 10 min, respectively. Firstly, the precursor α-$Co(OH)_2$ NSs are formed by electrodeposition with cyclic voltammetry (CV) technique, where the potential ranges from 1.2 V to 0.8 V with a scan rate of 0.05 V $s^{-1}$. The electrolyte of electrodeposition is 0.05 M $Co(NO_3)_2{\cdot}6H_2O$ solution. This electrodeposition process is performed in a three-electrode system by employing the CHI 660E electrochemical workstation (Chenhua Instruments, Inc. Shanghai). $Hg/Hg_2Cl_2$ (SCE) is selected as a reference electrode, a graphite plate is selected as a counter electrode, and a cleaned Ti mesh (1 cm × 4 cm) is selected as a working electrode. After 50 scanning cycles, the synthesized precursors α-$Co(OH)_2$ NSs are rinsed with ethanol and deionized water and dried at 60 °C overnight. To further attain Co-Bi NSs, a similar approach is adopted. The graphite plate is used as the counter electrode, SCE as the reference electrode and precursors α-$Co(OH)_2$/TM as the working electrode employing CV method in 0.1 M KBi until the current intensity stabilized.

### 2.2. Synthesis of $Mn_2O_3$ nanocubes

The preparation method of $Mn_2O_3$ nanocubes is based on reported literature with certain modifications [38]. Firstly, a 250 mL round bottom flask containing 40.0 mL of ultrapure water is heated to 85 °C. Then, PVP (1.1 g) dissolved in 13.0 mL of ethanol is added to the above hot water to form a homogeneous solution under stirring. $KMnO_4$ (0.372 g) dissolved in 15.0 mL of water is added to the above solution. The mixture is stirred at 85 °C for about 3 h. The obtained suspension is sealed in a 100 mL Teflon-lined autoclave, and a hydrothermal reaction occurs in an oven at 180 °C for 3 h. After cooling, the precipitate is centrifuged, rinsed with water and ethanol for 3 times and dried at 70 °C overnight.

### 2.3. Synthesis of $Mn_2O_3$@Au nanocube

Gold nanoparticles (AuNPs) are deposited on the synthesized $Mn_2O_3$ nanocubes by the deposition–precipitation (DP) method using urea as a precipitant. In a typical process, 15.0 mL of $HAuCl_4$ solution (2.43 mM) and 60 mL of deionized water form a homogeneous solution under continuous stirring, followed by the addition of 2.5 g of urea and 0.03 g of $Mn_2O_3$. The mixture is heated to 90 °C for 4 h. The suspension is centrifuged, rinsed three times with water, and dried under vacuum at 90 °C overnight.

### 2.4. Design of $Ab_2$-$Mn_2O_3$@Au nanocube

In short, 20.0 mg of $Mn_2O_3$@Au is dissolved in 2.0 mL of 0.1 M PBS solution (pH 7.4) and shaken for 1 h to form a suspension. Then, 1.0 mL of 20 μg $mL^{-1}$ labeled antibody ($Ab_2$-CEA) is added to the above suspension, and shaken for 12 h at 4 °C, in order to make the $Ab_2$-CEA and the Au NPs on the $Mn_2O_3$ nanocubes connected by the Au-N bonds as completely as possible, shown in Scheme 1B. Subsequently, 100 μL of 1 % BSA is added to block the non-specific binding sites. Finally, the suspension obtained above is centrifuged at 4000 rpm for 10 min, and then re-dispersed it in 2.0 mL of PBS (0.1 M, pH 7.4).

### 2.5. Construction of photoelectrochemical immunosensor

In this experiment, a highly sensitive PEC immunosensor for CEA determination is constructed based on Co-Bi NSs. And the construction process of PEC immunosensor is displayed in Scheme 1A. Firstly, a piece of TM coating with Co-Bi nanosheets (Co-Bi/TM) is prepared, and then it is immersed into a 5 mg $mL^{-1}$ polylysine solution (PLL) for 1 h to connect the antibody through the formation of amide bond. After drying in air naturally, it is immersed in a mixed solution of 75 mM EDC and 15 mM NHS for 1 h to activate the carboxyl group. After rinsed with water, the CoBi/PLL/EDC-NHS electrode is attained successfully. Then, 8 μL of 20 μg $mL^{-1}$ CEA-$Ab_1$ is connected to the surface of Co-Bi/PLL/EDC-NHS electrode at 37 °C. After hatching for 45 min, it is washed with deionized water to eliminate CEA-$Ab_1$ physically adsorbed on the surface. After that, 7 μL of 1 % blocking agent, BSA, is hatched on the prepared electrode at 37 °C for 45 min to block non-specific binding sites, and then is rinsed with deionized water. Subsequently, 8 μL of CEA antigen at distinct concentrations are added to the electrode and hatched at 37 °C for 45 min, then rinsed with deionized water. After specific binding of

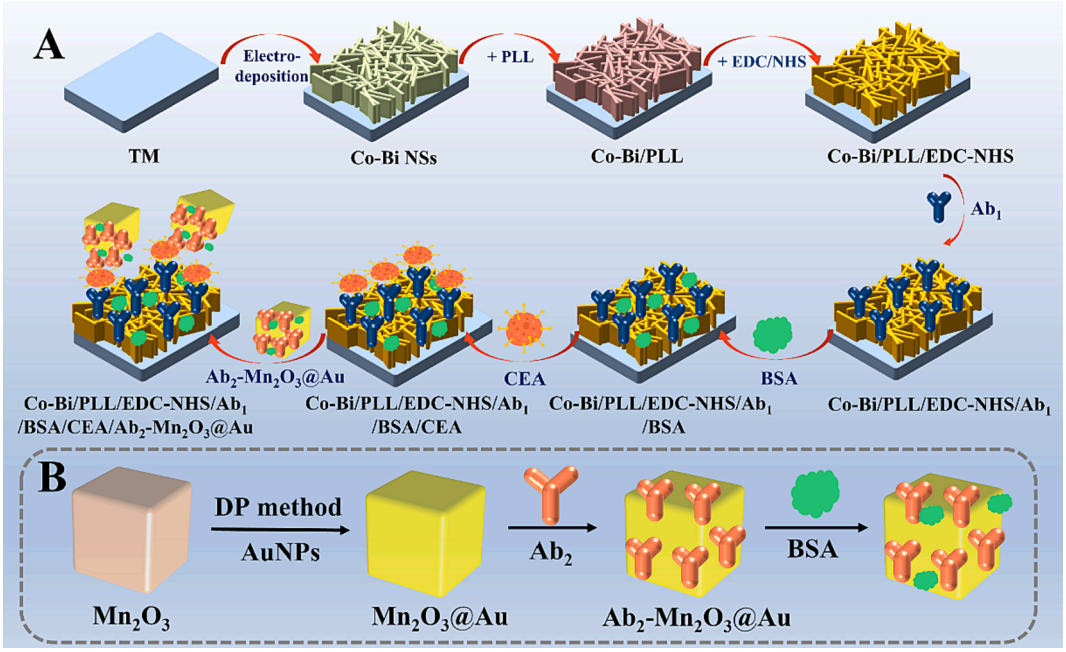


**Scheme 1.** Scheme diagram of (A) fabrication process of as-prepared PEC immunosensor for CEA determination. (B) preparation of the $Ab_2$-$Mn_2O_3$@Au.

CEA-$Ab_1$ and CEA, 15 μL of $Ab_2$-$Mn_2O_3$@Au suspension as a label, is hatched at 37 °C for 45 min, and is rinsed with deionized water. Finally, the electrode obtained above generates an $Ab_1$-CEA-$Ab_2$ sandwich PEC immunosensor for CEA detection. The immunosensor is stored in refrigerator at 4 °C for future use.

## 3. Results and discussion

### 3.1. Characterization of morphology and structure

The morphology of Co-Bi NSs is characterized by scanning electron

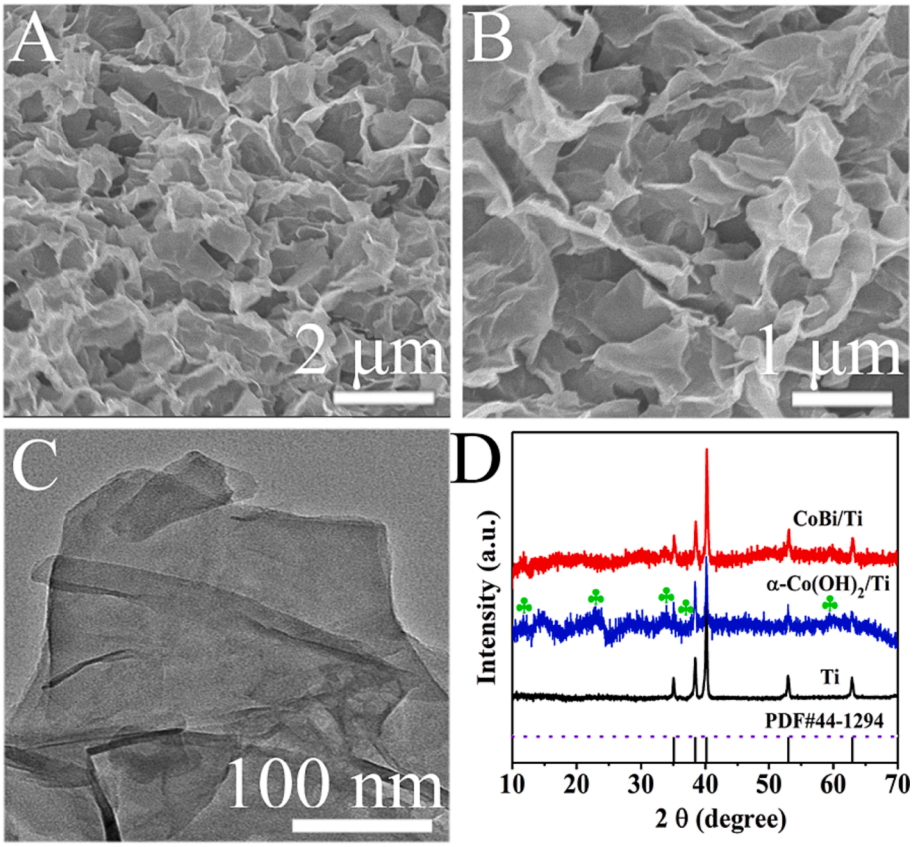


**Fig. 1.** Low (A) and high (B) SEM magnification images of Co-Bi NSs. (C) TEM image of Co-Bi NSs. (D) Powder XRD patterns of the bare Ti mesh, α-$Co(OH)_2$/Ti and Co-Bi/Ti.

microscopy (SEM) and transmission electron microscope (TEM). As displayed in Fig. 1A and B, the SEM images of Co-Bi indicate that TM has been completely covered by Co-Bi NSs. In addition, we find that the platelets of Co-Bi NSs are arranged in arbitrary orientation, providing a larger specific surface area for loading more photoactive nanomaterial. The TEM image of Co-Bi NSs, as shown in Fig. 1C, displays thin sheet-like structure with clearly distinguishable edges.

The crystallinity and phase purity of the obtained nanomaterials can be certified by X-ray diffractometer (XRD). As can be seen from Fig. 1D, the XRD patterns of bare Ti mesh (TM), α-$Co(OH)_2$/TM and Co-Bi/TM are characterized, with diffraction angles between 10° and 70°. The characteristic peaks at 35.09°, 38.42°, 40.17°, 53.00° and 62.95° are assigned to (100), (002), (101), (102) and (110) lattice planes of Ti (PDF 44-1294). The diffraction peaks at 11.54°, 23.20°, 33.54°, 38.14° and 59.08° are assigned to α-$Co(OH)_2$, respectively, which is consistent with the literature [29]. When the precursor α-$Co(OH)_2$ are tuned through electrochemical oxidation, we can only observe the characteristic peaks of the Ti in the XRD pattern, indicating the amorphous products of Co-Bi have been formed. In addition, we propose the possible mechanism for such a Co-Bi NSs [29]. During the cyclic voltammetry scanning, the Co species at the α-$Co(OH)_2$ surface is oxidized into a higher valence state. The in situ precipitation of Co-Bi on the α-$Co(OH)_2$ NSs is promoted via the electrostatic attractive interactions between such Co cations and borate anions in K-Bi solution. This process proceeds repeatedly until the complete conversion of α-$Co(OH)_2$ into Co-Bi NSs ultimately.

$Mn_2O_3$ nanocubes are synthesized by hydrothermal method. Fig. 2A and 2B display the morphology of $Mn_2O_3$ nanocubes by SEM and TEM, respectively. From above images, we can see that $Mn_2O_3$ nanocubes have been prepared successfully. It is clearly seen that the surface of $Mn_2O_3$ nanocube is very smooth in Fig. S1. In addition, the TEM image of $Mn_2O_3$@Au in Fig. 2C also reveals that Au NPs have been perfectly composited on the surface of the $Mn_2O_3$ nanocubes. The magnified TEM image of $Mn_2O_3$@Au shows a dense distribution of Au nanoparticles on its surface in Fig. S2.

In order to further determine the oxidation state of the synthesized manganese oxides, X-ray photoelectron spectroscopy (XPS) analysis is performed, which is the tool for determining the surface composition. Fig. 2D shows the spectrogram of Mn 2p, the two peaks at 641.1 eV and 652.8 eV are assigned to Mn $2p_{3/2}$ and Mn $2p_{1/2}$, respectively. The spin energy gap of Mn 2p is 11.7 eV, which is consistent with the value of $Mn_2O_3$ in the literature [39,40]. The spectrogram of Au 4f is presented in Fig. 2E, the binding energy of 84.5 eV and 88.2 eV are attributed to Au $4f_{7/2}$ and Au $4f_{5/2}$, respectively, indicating the formation of $Au^0$ [41].

The XRD patterns of $Mn_2O_3$ and $Mn_2O_3$@Au are displayed in Fig. 2F, with diffraction angles between 20° and 80°. The characteristic peaks at 23.13°, 32.95°, 35.68°, 38.23°, 40.62°, 42.95°, 45.18°, 47.30°, 49.35°, 53.27°, 55.19°, 57.03°, 58.84°, 60.62°, 62.37°, 64.08°, 65.81°, 67.46°, 69.11°, 70.74°, 72.35°, 73.95° and 75.55° are indexed to (211), (222), (321), (400), (411), (421), (332), (422), (431), (521), (440), (433), (600), (611), (620), (541), (622), (631), (444), (543), (640), (721) and (642) lattice planes of $Mn_2O_3$ (PDF 41-1442), respectively. When Au NPs are deposited on the surface of $Mn_2O_3$ by deposition–precipitation (DP) method, we can observe the characteristic peaks of Au NPs from the XRD pattern compared with $Mn_2O_3$, which indicated that Au NPs have been successfully compounded with $Mn_2O_3$.

### 3.2. Construction of PEC immunosensor

The PEC behavior of immunosensor is a potent method to characterize the property of electrode interface. Therefore, we carry out PEC tests to verify whether the prepared electrode is successfully fabricated step by step, as shown in Fig. 3A. Compared with Co-Bi NSs (curve a), the photocurrent response (curve b) is enhanced after PLL immobilizing on it subsequently, because of the good PEC property of PLL. When CEA antibody (CEA-$Ab_1$), BSA, and CEA antigens are sequentially loaded on the Co-Bi/PLL/NHS-EDC surface, the photocurrent response weakens little by little, corresponding to the curve d, e and f, separately. This is due to the nature of the biomacromolecule (CEA-$Ab_1$, BSA and CEA antigens) on the electrode surface that greatly hinders electron transfer. Then, the $Ab_2$-$Mn_2O_3$@Au complex is treated as label and captured on the electrode surface through the specific binding of antibody $Ab_2$ and antigen CEA. At this time, the photocurrent increases significantly (curve f), which testifies that the immunosensor is successfully manufactured, and on the other hand, the photocurrent signal is triumphantly amplified. These results obtained above keep pace with the fact that the electrodes are assembled as expected. And the novel immunosensor can enhance the analytical sensitivity of low-level protein detection. The corresponding histogram of different electrodes shown in Fig. 3B more clearly displays the situation described in Fig. 3A.

The possible mechanism of Co-Bi-$Mn_2O_3$@Au immunosensor is shown in Scheme 2. Under the light irradiation, the charge separations

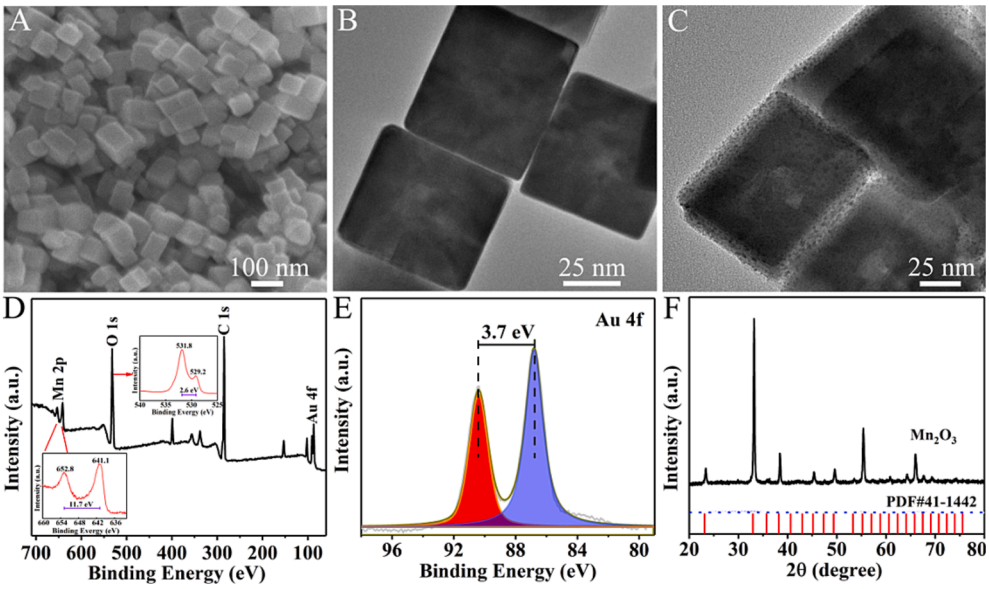


**Fig. 2.** (A) SEM image of $Mn_2O_3$ nanocubes. (B) TEM image of $Mn_2O_3$ nanocubes. (C) TEM image of $Mn_2O_3$@Au. (D) XPS survey of $Mn_2O_3$@Au. Inset: the Mn 2p and O 1s region of $Mn_2O_3$@Au. (E) The Au 4f region of $Mn_2O_3$@Au. (F) Powder XRD patterns of $Mn_2O_3$ nanocubes and compound $Mn_2O_3$@Au.

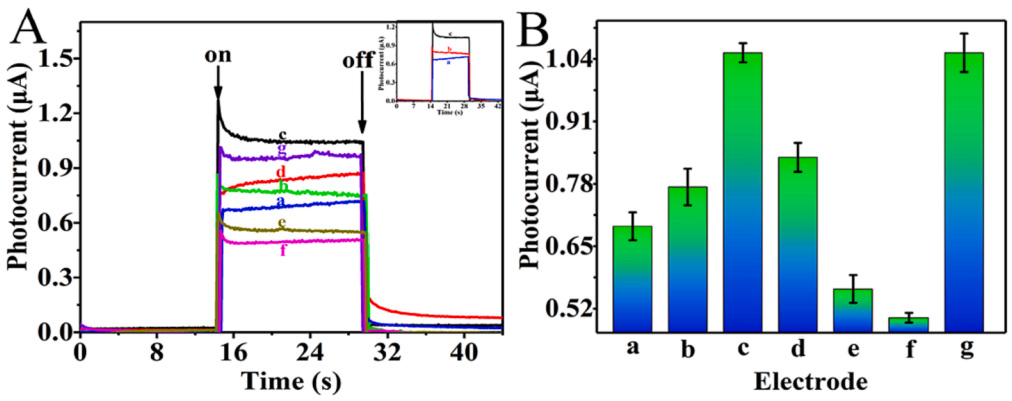


**Fig. 3.** (A) Photocurrent responses of the modified electrode: (a) Co-Bi NSs, (b) Co-Bi/PLL; (c) Co-Bi/PLL/NHS-EDC; (d) Co-Bi/PLL/NHS-EDC/CEA-$Ab_1$; (e) Co-Bi/PLL/NHS-EDC/CEA-$Ab_1$/BSA; (f) Co-Bi/PLL/NHS-EDC/CEA-$Ab_1$/BSA/CEA; (g) Co-Bi/PLL/NHS-EDC/CEA-$Ab_1$/BSA/CEA/$Ab_2$-$Mn_2O_3$@Au. Insert: (a) Co-Bi NSs, (b) Co-Bi /PLL; (c) Co-Bi/PLL/NHS-EDC. The concentration of CEA is 1.0 ng $mL^{-1}$. The PEC test is performed in 0.10 M PBS solution (pH 7.0) containing 2.0 mM AA, and applied voltage at 0.3 V. (B) The corresponding histogram of different electrode.

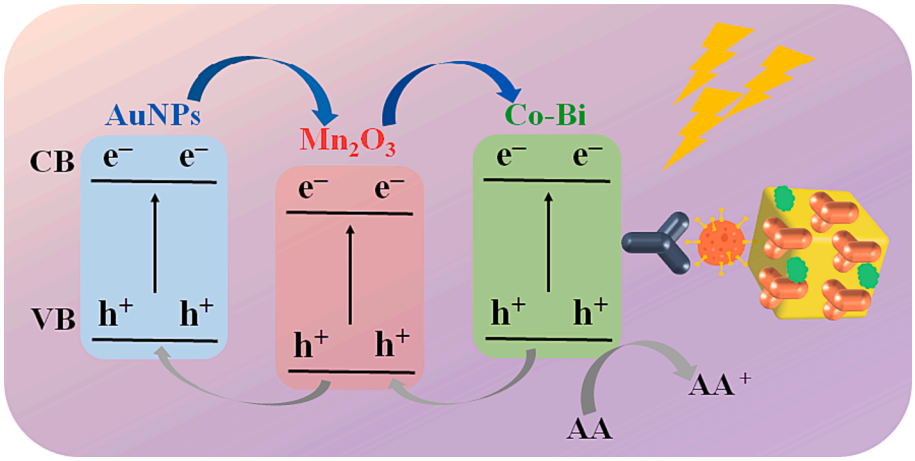


**Scheme 2.** Possible mechanism of Co-Bi-$Mn_2O_3$@Au immunosensor.

of Au NPs and $Mn_2O_3$ occur simultaneously. Co-Bi nanosheets absorb light resulting in photoexcited electron-hole pairs. The ascorbic acid acts as an electron donor for the photogenerated holes, changing the photocurrent intensity. As shown in Fig. 3A, Co-Bi NSs catalyzes the oxidation of AA to produce a current value (curve a). When Polylysine (PLL) is decorated on Co-Bi, the photocurrent value will increase because the carboxyl and amino groups of PLL undergo oxidation–reduction reactions (curve b). After the carboxyl and amino groups of PLL are activated by EDC-NHS, its redox reaction is more easily to occur, resulting in a stronger photocurrent value (curve c). When CEA-$Ab_1$ (curve d), BSA (curve e), and CEA (curve f) are modified on the Co-Bi/PLL/NHS-EDC nanosheets, the photocurrent value continuously increased, which indicates their successful assembly. This increase in photocurrent value could be ascribed to the fact that the proteins are nonconductive and the electron transfer could be impeded by the insoluble precipitated layer [42]. When $Ab_2$-$Mn_2O_3$@Au nanocubes are modified on the Co-Bi/PLL/NHS-EDC/CEA-$Ab_1$/BSA/CEA, the photoelectric current value will be greatly enhanced, because $Mn_2O_3$@Au nanocubes will oxidize AA and generate a photocurrent under light conditions.

### 3.3. Optimization of experimental conditions

In immunoassay, the experimental parameters have a great effect on the sensitivity of the prepared immunosensor during the process of fabrication and detection of antibody–antigen specific binding. Firstly, the influence of pH is investigated with PBS solution in the range of pH 5.7 ~ 8.0, as displayed in Fig. 4A. It can be seen that the photocurrent response reaches its maximum at pH 7.0, indicating that the performance is the best at this time. This may be due to the fact that the system is too acidic or alkaline to destroy the bioactivity of the protein [43]. Therefore, we choose pH 7.0 as the optimal pH for subsequent PEC testing. Then, the applied voltage has a great influence on the generation of the photocurrent signal, as displayed in Fig. 4B. The photocurrent amplified strongly as the applied potential increasing from 0 to 0.3 V. After that, the response weakens when a more positive voltage is applied. According to previous works, the intensity of resulting anodic photocurrent can be controlled by the applied potential. This maybe attribute to the destruction of the surface of CEA immunosensor by applying a high potential [44,45]. Thus, we choose 0.3 V as the application voltage for photoelectrochemical trials to achieve relatively higher photocurrent signals, and ultimately improve the sensitivity of the immunosensor.

As displayed in Fig. 4C, the effect of the amount on the PEC response is investigated by adding distinct volumes of $Ab_2$-$Mn_2O_3$@Au suspensions. As the volume of $Ab_2$-$Mn_2O_3$@Au suspensions increasing from 0.0 μL to 15.0 μL, the photocurrent response gradually enhances, and then, the suspension is continuously dropped until 20.0 μL, an obvious weaken is observed. The film thickness of the modified electrode surface can be changed by adding different volumes of $Ab_2$- $Mn_2O_3$@Au suspensions. The thicker the film, the more photoactive substances and light absorption it produces. However, the thicker the film on the

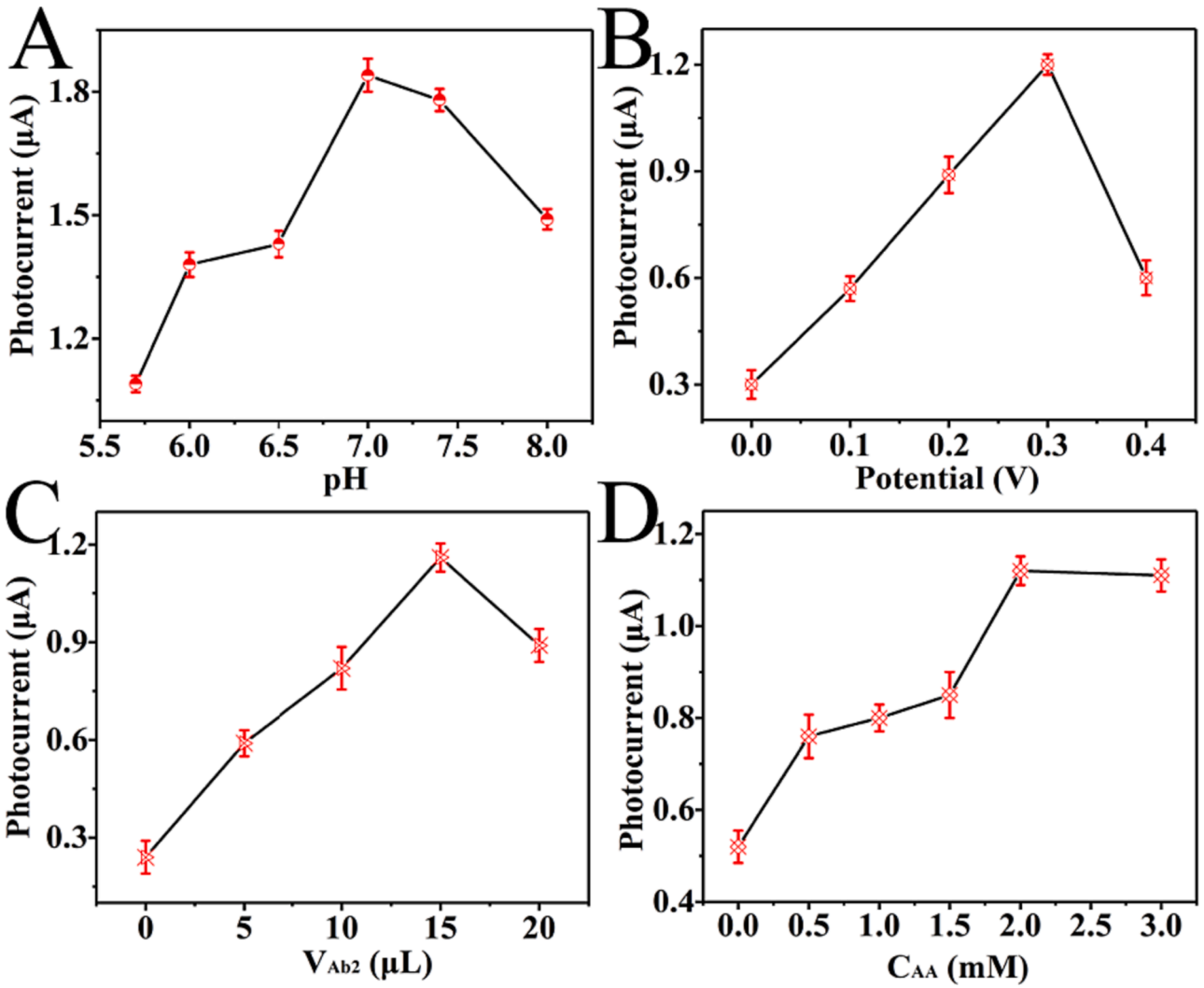


**Fig. 4.** The optimization of experimental parameters: the pH of the phosphate buffer solution (A), the effect of the applied voltage (B), the volume of $Ab_2$-CEA/$Mn_2O_3$@Au (C) and the concentration of AA (D) on the photocurrent responses.

electrode surface, the larger the diffusion resistance of electron movement, and the photocurrent attenuated accordingly [44]. Hence, we choose 15.0 μL of $Ab_2$-$Mn_2O_3$@Au suspension as the optimum volume for the subsequent tests.

Different concentration of AA has a vital effect on enhancing and stabilizing the photocurrent intensity. As a valid electron donor, AA can inhibit the aggregation of electrons and holes in $Mn_2O_3$@Au photosensitive electrodes. Fig. 4D displays the influence of different concentrations of AA on the photoelectric performance of the immunosensor. The signal is amplified strongly as the concentration of AA increased from 0 to 2.0 mM. After that, a larger concentration is added and the response remains constant. When the AA concentration is low (<2.0 mM), there are few reductant molecules that can be used to donate electrons to photo-generated holes, resulting in a decrease in electron output. As the AA concentration increasing (>2.0 mM), the absorbance of the solution system enhanced, ascribed to the saturation of the radiation intensity reaching the electrode surface, and the efficiency of excited $Mn_2O_3$@Au decreased. In addition, the response reaches a plateau at a high concentration (3.0 mM), which may also be caused by the saturation of electron donor [40]. Therefore, we opt 2.0 mM as the optimal concentration for the subsequent detection. The loading amount of the capture antibody and the detection antibody been optimized in Fig. S3. As shown in Fig. S3A, a significant enhancement of photocurrent is observed between 5 and 25 μg $mL^{-1}$ of anti-CEA. After the loading amount exceeds 20 μg $mL^{-1}$, the photocurrent signals gradually become stable, indicating that the amount of capture antibody on the electrode gradually reaches saturation. Therefore, 20 μg $mL^{-1}$ of capture antibody is the optimal amount. The same situation occurs in the optimization experiment of labeled antibody in Fig. S3B. Therefore, 20 μg $mL^{-1}$ of labeled antibody is the optimal amount.

### 3.4. *Quantitative determination of CEA*

Quantitative analysis of CEA is accomplished by observing the variation of photocurrent signal via employing PEC technology. As the concentration of CEA increased, higher electron transfer efficiency is achieved, which ultimately leads to an enhancement in photocurrent. It can be seen from Fig. 5A that the photocurrent intensity strengthens significantly as the CEA concentration enhanced. Fig. 5B displays the corresponding calibration plot of photocurrent versus $lgC_{CEA}$, where the relationship between photocurrent intensity and CEA concentration is logarithmic. The linear correlation is $I = 0.42 + 0.33\ lgC_{CEA}$ ($R^2 = 0.989$). The semilogarithmic relationship is satisfied. The error of the slope and the intercept is ± .149 and ±0.0278 in Fig. S4. As can be observed from Fig. 5B, the linear range is from 0.1 ng $mL^{-1}$ to 1000 ng $mL^{-1}$, and the lower detection limit (LOD) is 5 pg $mL^{-1}$ (S/N = 3).

The reasons for the superior performance of the immunosensor mainly involved the following aspects: (1) Co-Bi NSs possess a larger

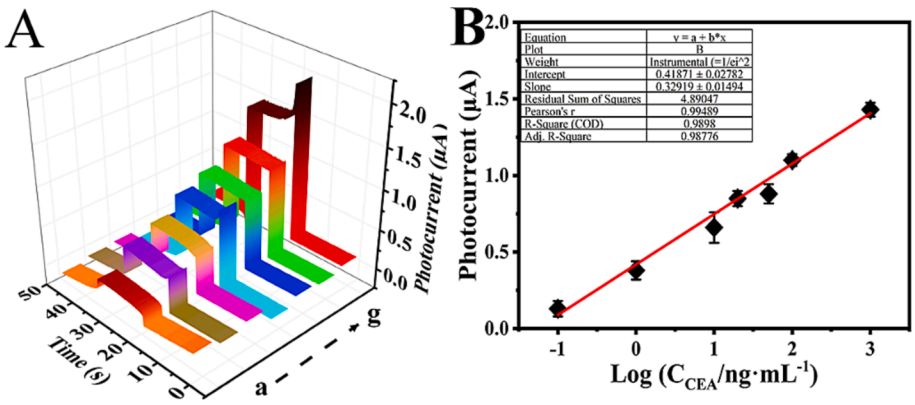


**Fig. 5.** (A) PEC responses of the immunosensor at different concentrations of CEA: (a) 0.1, (b) 1, (c) 10, (d) 20, (e) 50, (f) 100, (g) 1000 ng mL$^{-1}$. (B) The calibration plot of photocurrent versus CEA concentration, error bar RSD (n 3).

surface area, which allow more CEA-Ab$_1$ to be attached to the electrode. (2) A large number of Ab$_2$ are connected to the surface of $Mn_2O_3$@Au by Au NPs via Au-N bonds, improving the contact opportunities for antibody-antigen interactions. (3) High loading levels of AuNPs on $Mn_2O_3$ nanocubes promote photoelectrochemical activity. As displayed in Table S1, the means used in this experiment has certain superiority in CEA monitoring compared to previously reported means.

### 3.5. Analysis in real sample

Real serum samples are employed to verify the practicability of the signal amplification technology. And the human serum samples are diluted with 0.1 M PBS. As observed from Fig. 6A, the photocurrent intensity strengthens significantly as the CEA concentration enhanced, in the human serum. The inherent CEA concentration in the serum is measured by enzyme-linked immunosorbent assay (ELISA) and the results is 1.03 ng mL $^{1}$. The test in the serum is equivalent to an increase of 1.03 ng mL $^{1}$ at the corresponding concentrations. As displayed in Fig. 6B, the intensity of photocurrent has a good linear relationship with lg$C_{CEA}$ in diluted human serum, where the CEA concentration is from 10 pg mL $^{1}$ to 50 ng mL $^{1}$. An excellent linearity is achieved, in which the equation is $I = 1.51 + 0.44\ \lg C_{CEA}$ ($R^2 = 0.985$). The error of the slope and the intercept is ±0.0271 and ±0.0372 in Fig. S5. Above results indicate that as-prepared immunosensor is expected to be applied in practice.

In addition, the precision is investigated by applying standard addition method for recovery tests. Three serum samples are measured by adding CEA standard samples at different concentrations, and the

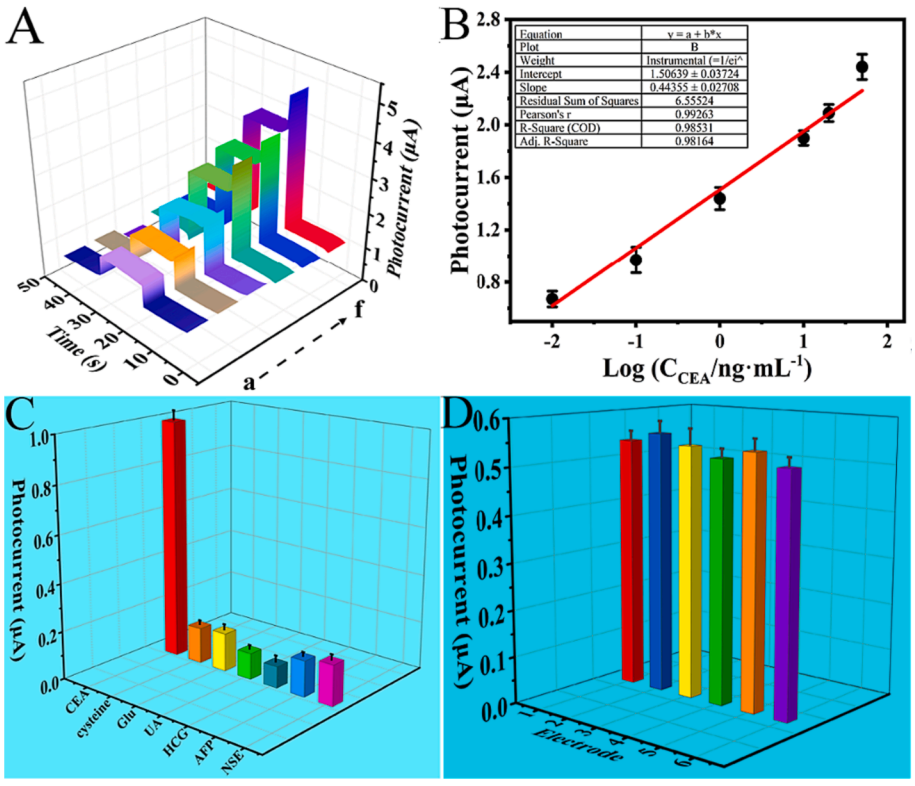


**Fig. 6.** (A) Photocurrent responses of the immunosensor at different concentrations of CEA: (a) 0.01, (b) 0.1, (c) 1, (d) 10, (e) 20, (f) 50 ng mL$^{-1}$ in the human serum. (B) Plot of photocurrent vs. CEA concentration, error bar RSD (n 3). (C) Specificity of the immunosensor: photocurrent responses to 1 ng mL$^{-1}$ CEA; 10 ng mL$^{-1}$ cysteine; 10 ng mL$^{-1}$ glutamate; 10 ng mL$^{-1}$ UA; 10 ng mL$^{-1}$ HCG; 10 ng mL$^{-1}$ AFP; 10 ng mL$^{-1}$ NSE, error bar RSD (n 3). (D) Reproducibility of six different electrodes. The PEC tests are performed in a human serum containing 2.0 mM AA with 0.3 V applied voltage, error bar RSD (n 3).

recoveries are within a reasonable scope, demonstrating the applicability of the immunosensor in real serum. Compared with ELISA method, the results received by the homemade immunosensor also display satisfactory feasibility performance for detection CEA in human serum.

### 3.6. Specificity, reproducibility and stability of the immunosensor

Non-specific adsorption is an urgent issue that needs to be solved in the process of constructing immunosensors, and it cannot be easily identified with specific binding, which ultimately affects the sensitivity. So, we conduct a specificity experiment to demonstrate that the observed photocurrents are caused by antibody-antigen specific interactions, rather than non-specific adsorption. As displayed in Fig. 6C, some biomarkers that may coexist in human serum are investigated. The immunosensor is hatched in 1 ng mL $^{1}$ CEA and 10-folds of the interferers, including 10 ng mL $^{1}$ of cysteine, glutamate (Glu), uric acid (UA), human chorionic gonadotropin (HCG), alpha fetal protein (AFP) and neuron specific endase (NSE), separately. Compared with the signal generated by pure CEA alone, the photocurrent generated by a single interfering protein is negligible, although their concentrations are much higher than CEA. And the photocurrent produced by all interfering substances does not exceed 12.5 % of the CEA. All these manifest that the photocurrent is largely generated by antibody-antigen specific binding, almost no notable non-specific adsorption interference, proving the excellent specificity of this signal multiplication strategy. The immunosensors prepared in the same and different days are tested in Fig. S6. The final electrode (Co-Bi/PLL/NHS-EDC/CEA-$Ab_1$/BSA/CEA/$Ab_2$-$Mn_2O_3$@Au) is tested by i-t curve at different time periods on the same day, as shown in Fig. S6A. After 9 h, this electrode still maintains 94 % of its initial activity. The electrode (Co-Bi/PLL/NHS-EDC/CEA-$Ab_1$/BSA/CEA/$Ab_2$-$Mn_2O_3$@Au) is evaluated over a period of ten days of storage (at 4 ℃). After six days and ten days, the photocurrent of the immunosensor decreases to approximately 91 % and 88 % of its initial value in Fig. S6B, respectively.

In order to verify the reproducibility of the as-prepared sensor, the test is performed on six individual electrodes under the equivalent test environment, and the CEA concentration is 1.0 ng mL $^{1}$. It can be concluded from Fig. 6D that the RSD is 2.13 %, which demonstrates the immunosensor possesses perfect accuracy and reproducibility. The stabilization of the PEC immunosensor is assessed through employing proposed biosensor to measure 1.0 ng mL $^{1}$ CEA. The photocurrent intensity is recorded under uninterrupted on/off radiation periods for 600 s. It can be seen from Fig. S7, no notable change in the photocurrent of PEC immunosensor employing $Ab_2$-$Mn_2O_3$@Au as label, and the response maintains at 93 % of the original signal after 600 s irradiation. The above results manifest the proposed PEC immunosensor possesses stable photocurrent to CEA detection.

## 4. Conclusion

In summary, as-constructed immunosensor realizes the qualitative and quantitative analysis of CEA through transforming the concentration of CEA into the detected PEC signal. Co-Bi NSs are used as the basal material to construct PEC immunosensor for the first time. The successful prepared Au@$Mn_2O_3$ nanocubes act as the probe, amplifying the signal of the biosensor. The antibody–antigen–antibody sandwich type PEC immunosensor is fabricated layer by layer fixation. Impressively, this PEC immunosensor has outstanding performance, a low detection limit, wide linear range, good specificity, stability and reproducibility. Moreover, it can be used in human serum detection. This strategy may be extended to construct other PEC platforms for the determination of biomarkers in the future work.

## CRediT authorship contribution statement

**Wenbo Lu:** Conceptualization, Data curation, Funding acquisition, Writing – original draft, Writing – review & editing. **Shoufeng Xue:** Methodology, Data curation. **Xuebo Liu:** Validation, Formal analysis, Writing – review & editing. **Cancan Bao:** Validation, Data curation. **Huanhuan Shi:** Methodology, Writing – review & editing.

## Declaration of Competing Interest

The authors declare that they have no known competing financial interests or personal relationships that could have appeared to influence the work reported in this paper.

## Data availability

The data that has been used is confidential.

## Acknowledgements

This work was supported by the National Natural Science Foundation of China (No. 21705103), the Applied Basic Research Project of Shanxi Province (No. 202103021224251), Scientific and Technological Innovation Projects in Shanxi Universities (No. 2019L0460), the Graduate Education Innovation Project of Shanxi Province (2021Y485), and the 1331 Engineering of Shanxi Province.

## References

[1] Q. Wu, N. Li, Y. Wang, Y. Liu, Y. Xu, S. Wei, J. Wu, G. Jia, X. Fang, F. Chen, X. Cui, A 2D transition metal carbide MXene-based SPR biosensor for ultrasensitive carcinoembryonic antigen detection, Biosens. Bioelectron. 144 (2019) 111697–111703.
[2] J. Sun, K. Cui, L. Li, L. Zhang, J. Yu, Visible-light-driven renewable photoelectrochemical/synchronous visualized sensing platform based on Ni: FeOOH/$BiVO_4$ photoanode and enzymatic cascade amplification for carcinoembryonic antigen detection, Sens. Actuators B Chem. 304 (2020) 127301–127307.
[3] Z.R. Zhou, D.W. Li, R.C. Qian, H. Ju, DNAzyme-powered DNA walker for cooperative expression imaging of mutant p53 and telomerase in cancer cells, Anal. Chem. 90 (2023) 4122–4130.
[4] R. Bano, N. Soleja, M. Mohsin, Genetically encoded FRET-based nanosensor for real-time monitoring of A549 exosomes: Early diagnosis of cancer, Anal. Chem. 95 (2023) 5738–5746.
[5] Y. Wu, X. Chen, X. Luo, M. Yang, C. Hou, D. Huo, Bimetallic organic framework Cu/UiO-66 mediated “fluorescence turn-on” method for ultrasensitive and rapid detection of carcinoembryonic antigen (CEA), Anal. Chim. Acta 1183 (2021), 339000.
[6] Y. Hua, X. Ren, H. Ma, D. Wu, X. Song, H. Wang, L. Yang, D. Fan, Q. Wei, Facile preparation of poly-(styrene-co-maleic anhydride) encapsulated Iridium(III) complexes as highly efficient electrochemiluminescence indicators for sensitive immunoassay of CYFRA 21–1, Anal. Chim. Acta 1274 (2023), 341512.
[7] M. Wang, M. Jang, P. Li, M. Yuan, C. Zhao, W. Lai, J. Li, C. Hong, Y. Qi, Construction of a competitive electrochemical immunosensor based on sacrifice of Prussian blue and its ultrasensitive detection of alpha-fetoprotein, Anal. Chim. Acta 1257 (2023), 341143.
[8] J. Han, Y. Li, J. Feng, M. Li, P. Wang, Z. Chen, Y. Dong, A novel sandwich-type immunosensor for detection of carcino-embryonic antigen using silver hybrid multiwalled carbon nanotubes/manganese dioxide, J. Electroanal. Chem. 786 (2017) 112–119.
[9] L. Shi, W. Zheng, H. Miao, H. Liu, X. Jing, Y. Zhao, Ratiometric persistent luminescence aptasensors for carcinoembryonic antigen detection, Mirochim. Acta 187 (2020) 615–625.
[10] Z. Pan, D. Yang, J. Lin, K. Shao, S. Shi, Y.J. Teng, H. Liu, Y. She, Autofluorescence free detection of carcinoembryonic antigen in pleural effusion by persistent luminescence nanoparticle-based aptasensors, Anal. Chim. Acta 1194 (2022) 339408–339416.
[11] F. Liu, J. Cao, Y. Wang, X. Fu, S. Ren, Y. Liu, A spatial-resolved electrochemiluminescence aptasensor for carcinoembryonic antigen detection in a double-check mode, Sens. Actuators B Chem. 276 (2018) 173–179.
[12] X. Gu, Z. She, T. Ma, S. Tian, H.B. Kraatz, Electrochemical detection of carcinoembryonic antigen, Biosens. Bioelectron. 102 (2018) 610–616.
[13] J. Guo, L. Song, M. Chen, F. Mo, W. Yu, Y. Fu, Schottky-functionalized Z-scheme heterojunction: Improved photoelectric conversion efficiency and immunosensing, Biosens. Bioelectron. 222 (2023) 115000–115006.

[14] M. Chen, J. Guo, F. Mo, W. Yu, Y. Fu, Highly sensitive photoelectrochemical immunosensor based on organic multielectron donor nanocomposite as signal probe, Anal. Chem. 94 (2022) 17039–17045.

[15] Z. Han, M. Luo, L. Chen, J. Chen, C. Li, A photoelectrochemical immunosensor for detection of α-fetoprotein based on Au-ZnO flower-rod heterostructures, Appl. Surf. Sci. 402 (2017) 429–435.

[16] X. Huang, Q. Lin, L. Lu, M. Li, D. Tang, $In_2O_3/CdIn_2S_4$ heterojunction-based photoelectrochemical immunoassay of carcinoembryonic antigen with enzymatic biocatalytic precipitation for signal amplification, Anal. Chim. Acta 1228 (2022) 340358–340364.

[17] Y. Gao, M. Li, Y. Zeng, X. Liu, D. Tang, Tunable competitive absorption-induced signal-on photoelectrochemical immunoassay for cardiac troponin I vased on Z-scheme metal-organic framework heterojunctions, Anal. Chem. 94 (2022) 13582–13589.

[18] B. Sun, J. Dong, L. Cui, T. Feng, J. Zhu, X. Liu, S. Ai, A dual signal-on photoelectrochemical immunosensor for sensitively detecting target avian viruses based on AuNPs/g-$C_3N_4$ coupling with CdTe quantum dots and in situ enzymatic generation of electron donor, Biosens. Bioelectron. 124 (2019) 1–7.

[19] Y. Qian, J. Feng, H. Wang, D. Fan, N. Jiang, Q. Wei, H. Ju, Sandwich-type signal-off photoelectrochemical immunosensor based on dual suppression effect of PbS quantum dots/$Co_3O_4$ polyhedron as signal amplification for procalcitonin detection, Sens. Actuators B Chem. 300 (2019) 127001–127008.

[20] C. Mao, L. Wu, Y. Wen, X. Tang, Z. Huang, L. Zhao, Photoelectrochemical immunosensor for carcinoembryonic antigen detection-an attempt for early cancer screening, Biosens. Bioelectron. 220 (2023) 114918–114926.

[21] J. Chen, J. Zhao, J. Feng, D. Wu, H. Ma, X. Ren, Q. Wei, H. Ju, Photoelectrochemical immunosensor based on a 1D $Fe_2O_3$/3D Cd-$ZnIn_{2.2}S_y$ heterostructure as a sensing platform for ultrasensitive detection of neuron-specific enolase, Anal. Chem. 94 (2022) 17396–17404.

[22] R. Zhang, D. Zheng, J. Chen, C. Zhang, C. Wang, Design of NiS@$Ni_3S_2$/CdS heterostructure with intimate contact interface for sensitive photoelectrochemical detection of lincomycin, Food Chem. 418 (2023) 136028–136036.

[23] Q. Lin, Z. Yu, L. Lu, X. Huang, Q. Wei, D. Tang, Smartphone-based photoelectrochemical immunoassay of prostate-specific antigen based on Co-doped $Bi_2O_2S$ nanosheets, Biosens. Bioelectron. 230 (2023) 115260–115266.

[24] L.V.L. Martoni, N.O. Gomes, T.M. Prado, M.L. Calegaro, O.N. Oliveira Jr., S.A. S. Machado, P.A. Raymundo-Pereira, Carbon spherical shells in a flexible photoelectrochemical sensor to determine hydroquinone in tap water, J. Environ. Chem. Eng. 10 (2022), 107556.

[25] X.P. Liu, J.S. Chen, C.J. Mao, B.K. Jin, A label-free photoelectrochemical immunosensor for carcinoembryonic antigen detection based on a g-$C_3N_4$/CdSe nanocomposite, Analyst 146 (2021) 146–155.

[26] J. Li, Y. Zhang, X. Kuang, Z. Wang, Q. Wei, A network signal amplification strategy of ultrasensitive photoelectrochemical immunosensing carcinoembryonic antigen based on CdSe/melamine network as label, Biosens. Bioelectron. 85 (2016) 764–770.

[27] P. Wang, G. Sun, L. Ge, S. Ge, X. Song, M. Yan, J. Yu, Paper-based photoelectrochemical immunosensing based on CdS QD sensitized multidimensional porous ZnO spheres promoted by carbon nanotubes, Chem. Commun. 49 (2013) 10400–10402.

[28] G. Wen, X. Yang, X. Xi, Cathode photoelectrochemical immunoassay based on analyte-induced formation of exciton trapping for carcinoembryonic antigen detection, J. Electroanal. Chem. 757 (2015) 192–197.

[29] L. Yang, D. Liu, S. Hao, R. Kong, A.M. Asiri, C. Zhang, X. Sun, A cobalt-borate nanosheet array: an efficient and durable non-noble-metal electrocatalyst for water oxidation at near neutral pH, J. Mater. Chem. A 5 (2017) 7305–7308.

[30] R. Ge, H. Du, K. Tao, Q. Zhang, L. Chen, Cobalt-borate nanoarray: An efficient and durable electrocatalyst for water oxidation under benign conditions, ACS Appl. Mater. Interfaces 9 (2017) 15383–15387.

[31] S. García-Dalí, J. Quílez-Bermejo, R. Karthik, R.L.S. Canevesi, M.T. Izquierdo, M. Emo, A. Celzard, V. Fierro, Easy and support-free synthesis of bimetallic borates for boosting the oxygen evolution reaction, ACS Appl. Energy Mater. 6 (2023) 3735–3744.

[32] C. Bao, R. Zhang, Y. Qiao, X. Cao, F. He, W. Hu, M. Wei, W. Lu, Au nanoparticles anchored on cobalt boride nanowire arrays for the electrochemical determination of prostate-specific antigen, ACS Appl. Nano Mater. 4 (2021) 5707–5716.

[33] Y.-L. Deng, A.-N. Chen, W. Li, S.-S. Xin, C.-Y. Pan, Exploration of the oxygen reduction reaction activity of four transition metal borates: synthesis, structure and characterization, Dalton Trans. 52 (2023) 4382–4388.

[34] X. Ji, L. Cui, D. Liu, S. Hao, J. Liu, F. Qu, Y. Ma, G. Du, A.M. Asiri, X. Sun, A nickel-borate nanoarray: A highly active 3D oxygen-evolving catalyst electrode operating in near-neutral water, Chem. Commun. 53 (2017) 3070–3073.

[35] H. Park, A. Encinas, J.P. Scheifers, Y. Zhang, B.P.T. Fokwa, Boron-dependency of molybdenum boride electrocatalysts for the hydrogen evolution reaction, Angew. Chem. Int. Ed. 56 (2017) 5575–5578.

[36] T. Tan, P. Han, H. Cong, G. Cheng, W. Luo, An amorphous cobalt borate nanosheet- coated cobalt boride hybrid for highly efficient alkaline water oxidation reaction, ACS Sustain. Chem. Eng. 7 (2019) 5620–5625.

[37] S.A. Ansari, N. Parveen, H.M. Kotb, A. Alshoaibi, Hydrothermally derived three-dimensional porous hollow double-walled $Mn_2O_3$ nanocubes as superior electrode materials for supercapacitor applications, Elexctrochim. Acta 355 (2020), 136783.

[38] J. Zhao, J. Nan, Z. Zhao, N. Li, Facile fabrication of novel Mn2O3 nanocubes with superior light-harvesting for ciprofloxacin degradation, Catal. Commun. 102 (2017) 5–8.

[39] P. Pal, A.K. Giri, S. Mahanty, A.B. Panda, Morphology-mediated tailoring of the performance of porous nanostructured $Mn_2O_3$ as an anode material, CrystEngComm 16 (2014) 10560–10568.

[40] B. Saha, S.K. Jana, S. Majumder, B. Satpati, S. Banerjee, Selective growth of Co-electrodeposited $Mn_2O_3$-Au spherical composite network towards enhanced non-enzymatic hydrogen peroxide sensing, Electrochim. Acta 174 (2015) 853–863.

[41] B. Leng, L. Zou, J. Jiang, H. Tian, Colorimetric detection of mercuric ion (Hg2+) in aqueous media using chemodosimeter-functionalized gold nanoparticles, Sens. Actuators B Chem. 140 (2009) 162–169.

[42] J. Wang, J. Bei, X. Guo, Y. Ding, T. Chen, B. Lu, Y. Wang, Y. Du, Y. Yao, Ultrasensitive photoelectrochemical immunosensor for carcinoembryonic antigen detection based on pillar[5]arene-functionalized Au nanoparticles and hollow PANI hybrid BiOBr heterojunction, Biosens. Bioelectron. 208 (2022), 114220.

[43] V. Cappello, L. Marchetti, P. Parlanti, S. Landi, I. Tonazzini, M. Cecchini, V. Piazza, M. Gemmi, Ultrastructural characterization of the lower motor system in a mouse model of krabbe disease, Sci. Rep. 6 (2016) 1–15.

[44] Y.J. Li, M.J. Ma, J.J. Zhu, Dual-signal amplification strategy for ultrasensitive photoelectrochemical immunosensing of alpha-fetoprotein, Anal. Chem. 84 (2012) 10492–10499.

[45] Y. Shi, T. Li, L. Zhao, Y. Liu, K. Ding, D. Li, P. He, D. Jiang, J. Liu, H. Zhou, Ultrathin MXene nanosheet-based $TiO_2$/CdS heterostructure as a photoelectrochemical sensor for detection of CEA in human serum samples, Biosens. Bioelectron. 230 (2023), 115287.